communications earth & environment

Article

https://doi.org/10.1038/s43247-024-01764-2

Warming could shift the phenological responses of benthic microalgae in temperate intertidal zones

Raphaël Savelli[1,2] ✉, Vincent Le Fouest[2], Mélanie Becker[2], Garance Perrois[3], Fabienne Rousset[4] Christine Dupuy[2], Marc Simard[1] & Dimitris Menemenlis[1]

Intertidal mudflats colonized by sediment-dwelling microphytobenthos deliver a wide range of ecosystem services. Here we simulate the response of microphytobenthos, located on a temperate tidal mudflat along the French Atlantic coast in Northwestern Europe, exposed to changes in light, temperature, and sea level conditions predicted by the Intergovernmental Panel on Climate Change. Without sea level rise, microphytobenthos benefit from the balancing effect of net primary production fluctuations, experiencing an increase in winter and a decrease in summer. Under the worst emissions scenario, microphytobenthos bloom up to 14 days earlier in spring and 5 days later in fall, thereby extending the low-level microphytobenthos biomass period by an additional 3 weeks in summer. Sea level rise reduces light exposure leading to a pronounced decline in microphytobenthos under the medium-low emissions and worst emissions scenarios. We provide evidence that the anticipated warmer climate and sea level rise will have an impact on microphytobenthos, potentially triggering cascading effects across the entire food web and disrupting ecosystem services.

Tidal mudflats are distributed globally (Fig. 1), providing flood protection, water quality, and food production for millions of people[1–3]. They host very productive mats of sediment dwelling micro-algae, or microphytobenthos (MPB), inhabiting the top few micrometers of the sediment. MPB mats can produce daily as much organic carbon as phytoplankton do in coastal waters[4–7]. They foster numerous ecosystem services within the land-to-ocean interface[8,9], including CO_2 removal potential[10]. They provide the most important energy source for consumers of the benthic microfauna, meiofauna, macrofauna to birds and fishes, and thus support to the whole food web[9,11]. The high MPB production on mudflats contributes to the development of shellfish farming, in particular oyster and mussel that largely feed on MPB[12,13]. As tidal MPB only develop during low tides in emerged sediments directly exposed to atmosphere, net primary production (NPP) is driven by sharp and rapid changes in downwelling irradiance and mud surface temperature (MST)[14]. MPB can take advantage of high light and temperature conditions until a certain threshold beyond which photo- and thermoinhibition can occur. Such a high sensitivity to the radiative forcing raises concerns on how MPB standing stock and production will respond to climate change, and on their subsequent capacity to keep sustaining the entire food chain that relies upon to them.

As pelagic ecosystems are less subject to short-term variations of environmental conditions, oceans models are proving to be an effective solution for estimating phytoplankton response to future climate change[15,16]. Bridging the terrestrial and oceanic realms, tidal mudflats are swept by tides limiting MPB growth to just a few hours per day. This dynamics cannot be resolved by predictive models using daily meteorological forcings. We use hourly meteorological forcings simulated by 11 General Circulation Models and Regional Circulation Models (GCM-RCM; Table 1) of the Coupled Model Intercomparison Project - Phase 5 (CMIP5)[17,18]. The 11 GCM-RCM were forced by land-ocean surface and atmospheric data depicting trajectories of greenhouse gases concentrations based on observations (historical, 1950–2005) and on two Representative Concentration Pathways scenarios (RCP 4.5 and RCP 8.5, 2006–2099) from the Intergovernmental Panel on Climate Change (IPCC) Assessment Report Five (AR5). RCP 4.5 is a stabilization scenario meaning that the radiative forcing level stabilizes at 4.5 W m^{-2} before 2100. The RCP 8.5 scenario reflects greenhouse gas

[1]Jet Propulsion Laboratory, California Institute of Technology, 4800 Oak Grove Dr., Pasadena, CA, 91109, USA. [2]LIttoral, Environnement et SociétéS (LIENSs) - UMR 7266, CNRS-La Rochelle Université, 2 rue Olympe de Gouges, La Rochelle, 17000, France. [3]Tropical & Subtropical Research Center, Korea Institute of Ocean Science & Technology, 321-6 Haengwon-ri, Jeju, 63349, Republic of Korea. [4]Direction de la Climatologie et des Services Climatiques, Météo-France, Toulouse, France. ✉e-mail: raphael.savelli@jpl.nasa.gov

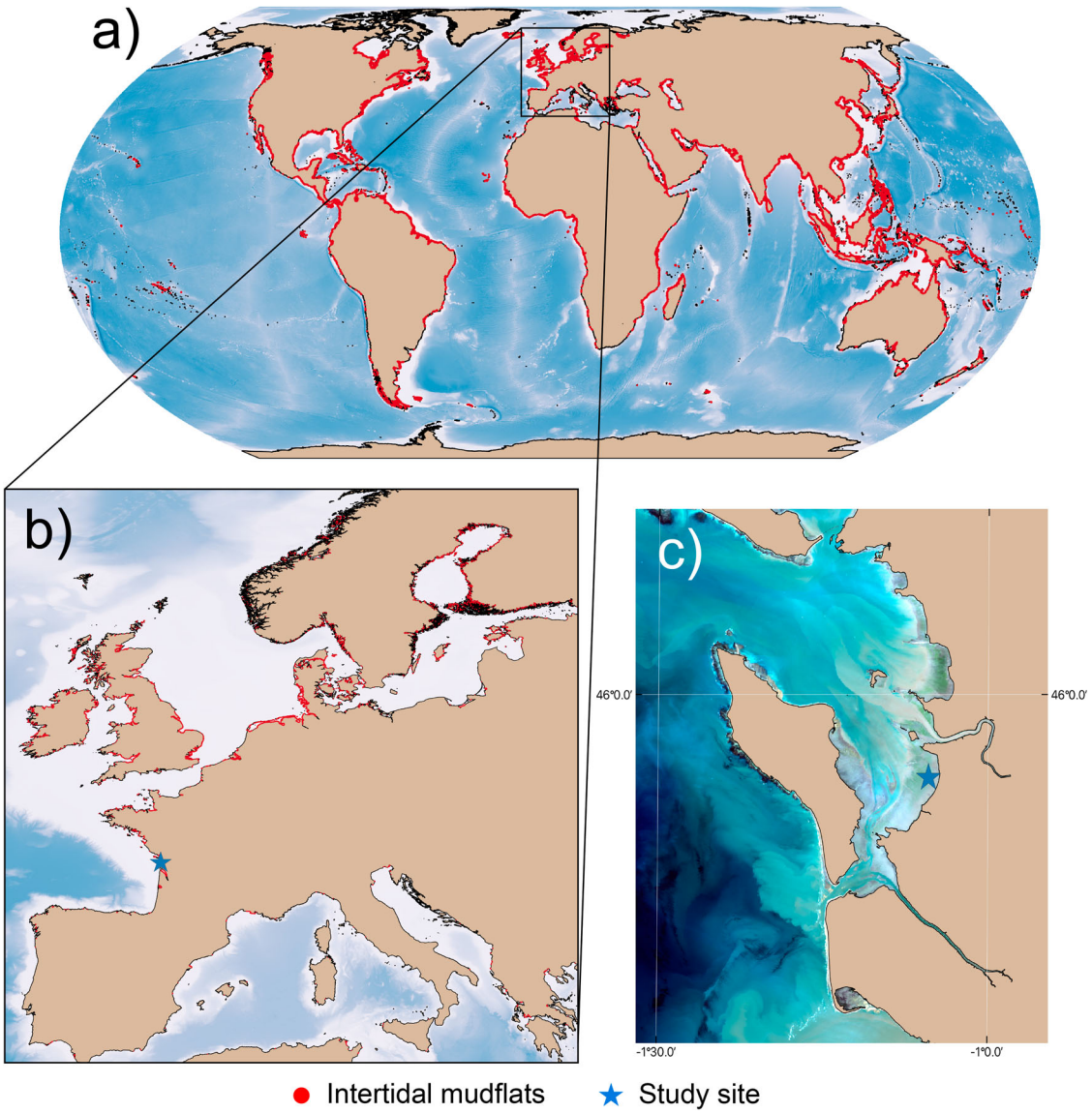

Fig. 1 | Overview of tidal mudflats: global, european, and regional perspectives. **a** Global distribution of tidal mudflats[83]. **b** Location of European tidal mudflats. **c** The semi-enclosed area of the Pertuis Charentais (France). The blue star indicates the model study site, a temperate tidal mudflat located along the French Atlantic coast of Northwestern Europe[6]. Bathymetry (in blue) is from the Generate Bathymetry Charts of the Ocean (GEBCO) product version 2023[84]. The true color image in (**c**) is a Sentinel-2 L2A scene from April 8, 2023 (modified Copernicus Sentinel data 2024/Sentinel Hub).

Table 1 | GCM-RCM pairs and simulated years

GCM	RCM	Historical	RCP 4.5	RCP 8.5
CNRM-CM5	Aladin63 V2	1952–2005	2006–2099	2006–2099
IPSL-CM5A-MR	WRF381P	1952–2005	2006–2099	2006–2099
IPSL-CM5A-MR	RCA4	1971–2005	2006–2099	2006–2099
HadGEM2-ES	RegCM4-6	1972–2005	–	2006–2098
HadGEM2-ES	CCLM4-8-17	1951–2005	2006–2098	2006–2098
EC-EARTH	Racmo22E v2	1951–2005	2006–2099	2006–2099
EC-EARTH	RCA4	1971–2005	2006–2099	2006–2099
MPI-ESM-LR	CCLM4-8-17	1951–2005	2006–2099	2006–2099
MPI-ESM-LR	REMO	1971–2005	2006–2099	2006–2099
NorESM1-M	HIRHAM5 v3	1952–2005	2006–2099	2006–2099
NorESM1-M	REMO	1951–2005	–	2006–2099

emissions that continue to rise throughout the 21st century, leading to a radiative forcing of 8.5 W m^{-2}; known as a worst-case scenario[19,20].

We used hourly meteorological data simulated by the GCM-RCM and hourly water level data to force a 2-layer physical-biological model of MPB and its principal grazer, a small gastropod inhabiting the mud surface[6,7,21,22] (see "Methods" section). We incorporated water level data both with and without accounting for sea level trends across the historical period and under the two RCP scenarios. The model simulated the production rate and biomass of both MPB and its grazer from 1951 to 2005 (historical run) and from 2006 to 2099 (RCP 4.5 and RCP 8.5 runs) for a large temperate tidal mudflat located along the French Atlantic coast in Northwestern Europe (Fig. 1). As a large macrotidal system made up of fine cohesive sediments, this site is largely dominated by MPB and experiences a wide range of environmental conditions that make it a suitable model for understanding how MPB is coping with environmental changes and stressors on temperate tidal flats, globally[6,7,21,22]. We estimated trends from the models ensemble mean and

analyzed trajectories taken by MPB PP and phenology in response to future conditions in downwelling irradiance, MST and grazing.

Results and discussion

MPB net primary production significantly decreases in the RCP 8.5 scenario

In the absence of sea level rise, both historical and RCP 4.5 scenarios showed no significant trends in downwelling irradiance experienced by MPB or NPP ($p > 0.01$) (Fig. 2a, b, e, f). In contrast, NPP significantly decreased over 2006–2099 in the most pessimistic scenario RCP 8.5 (-0.07 ± 0.05 g C m^{-2} yr^{-1}, $p < 0.01$) (Fig. 2e, f). This decline was however limited to a 4% reduction from the average annual NPP simulated over the historical period (172 ± 0.77 g C m^{-2} yr^{-1}). The decrease of NPP in RCP 8.5 was driven by MST that rose twice as much ($+0.04 \pm 0.004$ °C yr^{-1}, $p < 0.001$) as in the historical and RCP 4.5 scenarios ($+0.02 \pm 0.004$ °C yr^{-1}, $p < 0.001$) and by increasing grazing pressure reflected by increasing secondary production ($+0.03 \pm 0.02$ g C m^{-2} yr^{-1}, $p < 0.05$; (Fig. 2c, d, g, h). Conversely, the decrease of NPP became significantly more pronounced with the inclusion of sea level rise in both RCP scenarios (Fig. 2m, n). In RCP 8.5, NPP declined until it reached a tipping point occurring in 2065, i.e., 29 years earlier than in RCP 4.5 (Fig. 2m, n). Beyond this tipping point, a negative feedback occurred where a reduced exposure of MPB to irradiance due to shorter low-tide emersion periods (Fig. 2i, j) combined with the simulated MPB physiological response. In the model, the mean time spent by MPB cells at the sediment surface was set according to the time before the induction of photoinhibition (γ, 1 h). Beyond this time, the MPB cells that formed the biofilm at the surface migrated down within the sediment and gave room to other cells to migrate upwards into the biofilm. Combined with the MPB biomass in the sediment before the emersion period, γ set the potential duration of the biofilm at the sediment surface, or the productive period (γ^*, h; Eqs. (12) and (13)). As the MPB biomass decreased, the shorter the time spent by the cells at the sediment surface, the lower the NPP. Consequently, NPP became insufficient to support growth, leading to an irreversible decline of both MPB and grazers across both RCP scenarios (Fig. 2o, p).

The critical effect of light and temperature was previously reported to explain either a positive or negative response of oceanic NPP to global warming[23,24]. While studies have documented the short-term impacts of temperature and thermoinhibition on MPB during summer[6,25,26], there remains a gap in understanding the long-term consequences of rising temperatures on MPB dynamics. Our model demonstrates that, in the absence of sea level rise, light and MST exert only a limited influence on MPB net primary production over the course of decades. This scenario might also apply even with sea level rise if MPB can relocate upward on the mudflat and encounter comparable growth conditions. However, it becomes clear that sea level rise plays a pivotal role in shaping future net primary production of MPB, primarily by substantially reducing their access to light. This response underscores the importance of integrating such a factor into future modeling studies and management frameworks. In addition, tidal flats experience wave action induced by local winds and swells, leading to significant MPB resuspension[7]. When coupled with rising sea levels, anticipated alterations in the wave regime[27,28] might exacerbate the adverse trends simulated in our model, leading to direct erosion, fragmentation, and habitat loss for MPB, thus accentuating the amplification of negative impacts.

Furthermore, global warming can alter the biogeochemistry of sediment porewater in various ways. Firstly, elevated CO_2 levels and subsequent dissolution in seawater can enhance MPB photosynthetic activity and biomass[29–31]. However, MPB could become more susceptible to grazing as diatom frustules weaken in increasingly acidic waters[32]. Secondly, since most tidal mudflats are situated near river mouths and receive terrigenous nutrients drained from watersheds, ongoing alterations in nutrient loads and stoichiometry[33–35] can modify sediment biogeochemistry. Lastly, rising air temperatures could reshape the microbial species composition within mudflat sediments, consequently affecting organic matter remineralization rates[36]. Hence, incorporating MPB models into a comprehensive 3D physical framework that encompasses diagenetic sediment processes would help alleviate uncertainties linked to potential alterations in sediment biogeochemistry and MPB response in the future.

Global warming alters the phenology of MPB

In the scenario without sea level rise, the simulated annual trends in NPP resulted from marked seasonal patterns of both physical and biological

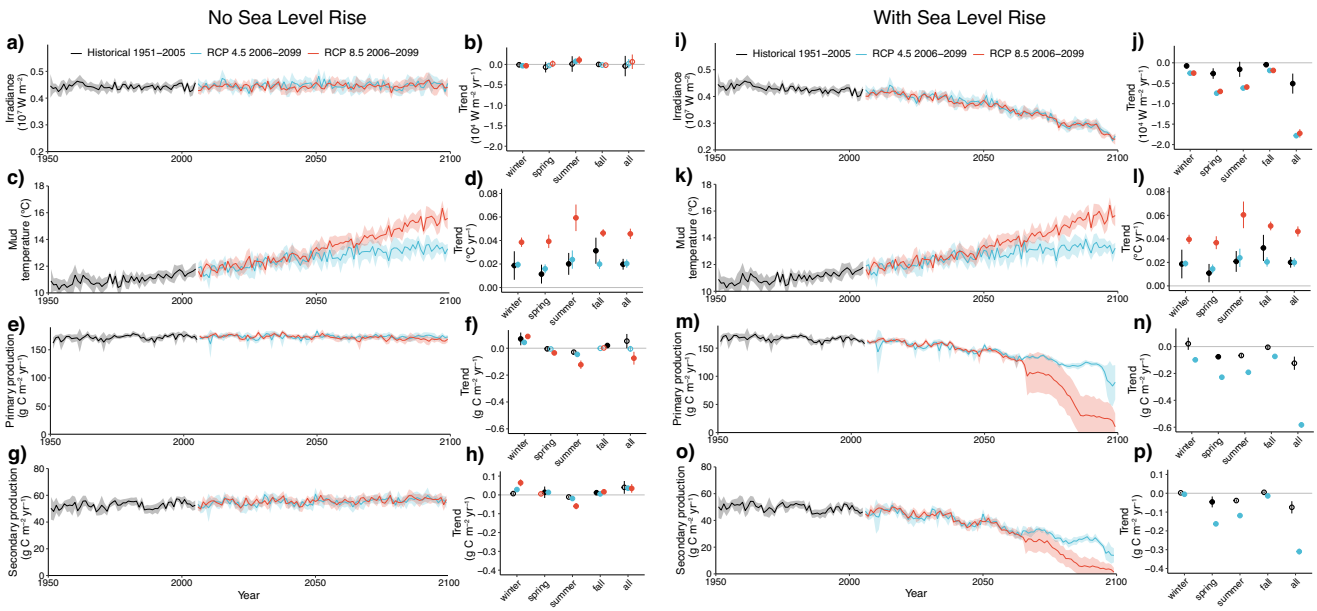

Fig. 2 | Simulated physical and biological conditions at the mud surface with and without sea level rise over 1950–2099. Yearly and low tide integrated irradiance (**a**, **i**), yearly averaged mud surface temperature (**c**, **k**), annual net primary production (**e**, **m**), annual secondary production (**g**, **o**), and associated seasonal trends (**b**, **d**, **f**, **h**, **j**, **l**, **n**, **p**) across the historical (black) and RCP 4.5 (blue) and 8.5 (red) scenarios. Shaded areas and error bars are confidence intervals at 95% from the GCM-RCM ensemble. Filled circles indicate significant trends (Mann-Kendall test). The absence of trend marks in the NPP and secondary production panels for the RCP 8.5 scenario with sea level rise (**n** and **p**) indicate a sharp, step-like decline in the time series, rendering trend estimates and statistical significance unreliable.

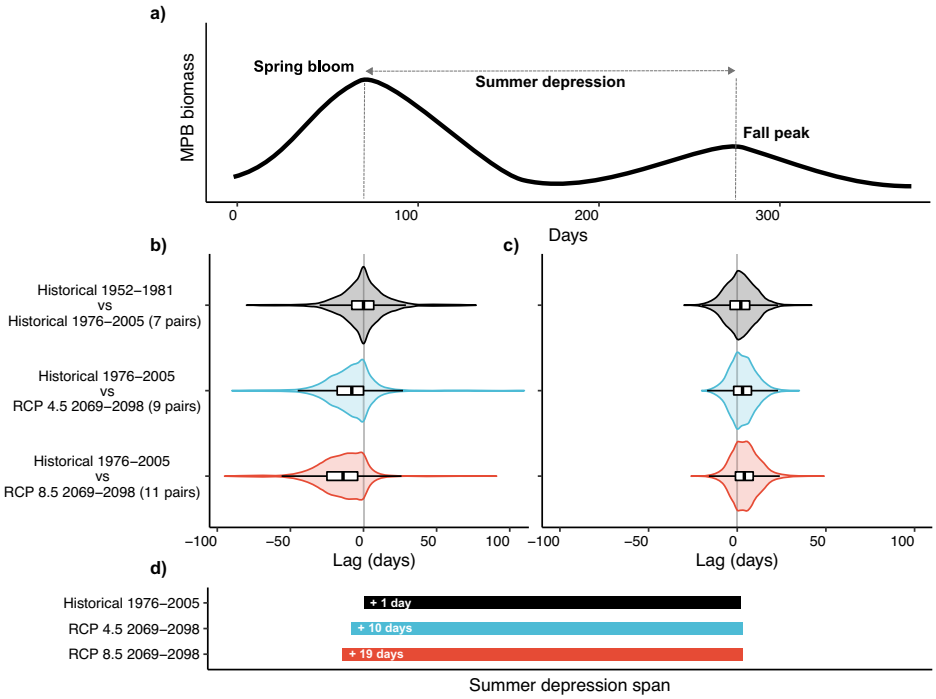

Fig. 3 | Phenological shifts in MPB biomass without sea level rise. a Conceptual seasonal cycle of MPB biomass with main characteristics based on ref. 6 and (**b**, **c**), interannual lag (days) from year-to-year cross-correlation between the beginning (1952–1981) and the end of the historical scenario (1976–2005) (black), between the end of historical scenario (1976–2005) and RCP 4.5 (2069–2099) (blue), and between the end of historical scenario (1976–2005) and RCP 8.5 (2069–2099) (red) for the spring and fall blooms, respectively. **d** Subsequent median change of the summer depression duration according to the historical (1975–2005), RCP 4.5 and 8.5 scenarios (2069–2099). Width of violin plots corresponds to the density of data in corresponding regions. Boxplots show the median, interquatile range and minimum and maximum.

conditions (Fig. 2). In winter, a significant and positive trend in MST was responsible for the increase of NPP at this season in all scenarios ($p < 0.001$) (Fig. 2c–f). With warmer winters, MST got closer to the temperature optimum for MPB photosynthesis. The pattern reversed in spring and summer, when daily MST exceeded the MPB temperature optimum causing a decrease in NPP. This simulated thermoinhibition of NPP was particularly pronounced in summer in RCP 8.5, where the highest increase in MST ($+0.06 \pm 0.01$ °C yr^{-1}, $p < 0.001$) coincided with the highest decline in NPP (-0.12 ± 0.03 g C m^{-2} yr^{-1}, $p < 0.001$) (Fig. 2c–f). Warmer springs and summers increased thermoinhibition of MPB photosynthesis, leading to a subsequent decline in NPP and biomass. In warm temperate mudflats like those in Southern Europe, thermoinhibition is the key factor responsible for the observed summer minimum in MPB biomass[25,26].

In addition, MPB are reported to face a substantial grazing pressure during the summer[6,37–40]. Contrary to NPP, our results suggest that grazer secondary production significantly increased in all scenarios (Fig. 2g). The metabolic theory of ecology states that temperature stimulates more the heterotrophic feeding, growth, and reproduction than photosynthesis[41,42]. A stronger grazing pressure on benthic diatoms as MST increases was previously reported on a mudflat in Northern Europe[39]. In the model, the grazing rate was constrained by both the MST and MPB biomass. As grazing was set in the model to increase or reach a plateau with rising MST (Eq. 16), the decline of secondary production in summer was due to the decrease of MPB NPP (Fig. 2g, h). The significant increase of annual secondary production in RCP 4.5 ($+0.03 \pm 0.02$ g C m^{-2} yr^{-1}, $p < 0.05$) and RCP 8.5 ($+0.03 \pm 0.02$ g C m^{-2} yr^{-1}, $p < 0.05$) was due to higher MST that sustained *Peringia ulvae* grazing in the absence of a substantial decline of MPB biomass. As a result, the carbon transfer from MPB to the benthic grazers remained efficient under warmer climate conditions (Fig. 2g, h). In the model, we only consider the gastropod *Peringia ulvae* as the dominant MPB grazer. However, intertidal mudflats may be dominated by other benthic fauna, such as bivalves[43] or crustaceans[44]. Hence, the response of predator-prey interactions, and consequently, NPP and secondary production, will be dependent on grazing pressure and the seasonal synchronicity between MPB and its consumer.

In marine systems, changes in plankton phenology can trigger negative cascading effects on higher trophic levels[45]. We used year-to-year lagged cross-correlations between the historical and RCP scenarios to identify shifts in the spring and fall MPB blooms without sea level rise (Fig. 3a). The onset of the spring bloom occurred earlier in RCP 4.5 (−8 days) and 8.5 (−14 days) ($p < 0.001$; Fig. 3b). In contrast, the fall bloom was delayed by 2 to 5 days, respectively (Fig. 3c). It resulted that the summer depression in biomass extended 11 days (RCP 4.5) to 18 days (RCP 8.5) ($p < 0.001$; Fig. 3d). Because of the steady downwelling irradiance over the 21st century, the higher MST was therefore responsible for the substantial shift of the bloom phenology. This is very consistent with a study that identifies warmer conditions as a major driver in future shifts in phytoplankton phenology at mid-latitudes[46].

A temporal mismatch between the available MPB biomass and requirements of grazer life stages can decrease secondary production and then the carbon transfer to higher trophic levels[47]. Temperature-driven changes in planktonic and benthic fauna species phenology from days to months were previously observed[48–51]. However, the simulated increase of MPB PP in winter might unexpectedly be detrimental for shellfish farming. When exposed to supplemented food resources during winter, oysters allocate more energy for gametogenesis at the expense of their immune system, making them more vulnerable in the spring and summer seasons[52]. In addition, tidal mudflats are critical stopover and wintering sites for migratory shorebirds that feed on benthic macrofauna and meiofauna[53,54]. Stopovers in migratory birds are often associated to optimal resource availability at a specific site[55]. Due to the complexity of coastal food webs, the impacts may vary across migratory shorebird species. While a change in the seasonal peak biomass of benthic grazers could pose a threat to species reliant on benthic fauna[56], this may not hold true for those that primarily consume MPB directly[57,58].

Conclusion

Our study draws future trajectories of intertidal microphytobenthic NPP in light of the RCP 4.5 and 8.5 scenarios, with and without sea level rise. The model shows that mud surface temperature keeps increasing over the next decades. In a scenario where there is no sea level rise, or if sea level do rise but the biofilm is capable of migrating upward on the mudflat to find similar growth conditions, MPB cope with a warmer climate, limiting the projected NPP decrease to less than 0.1 g C m^{-2} yr^{-1}. However, the onset of the MPB spring bloom occurs 8 to 14 days earlier in the future. Meanwhile, as secondary production increases with temperature in both scenarios, the carbon

transfer from MPB to their benthic primary consumer, gastropod *Peringia ulvae*, is maintained but cascading effect throughout the entire food web remains to be assessed. In contrast, we show that sea level rise has dramatic consequences on future trends of MPB net primary production, primarily by substantially reducing their access to light. Therefore, we underscore the critical importance of integrating sea level rise into our analyses and emphasize the necessity of considering this aspect in future research endeavors. Given the very dynamic nature of intertidal mudflats, sustained efforts are required to make model predictions more realistic. This entails incorporating a comprehensive understanding of changes in geomorphology, hydrodynamics, sediment biogeochemistry, and biological communities into future modeling framework. As MPB play a crucial role in the productivity and support of associated upper trophic levels within tidal mudflats, this approach can serve as a stepping stone to a more holistic assessment of how land-ocean interface ecosystems will cope with climate change. Recognizing the potential role of tidal flats in global carbon fluxes, implementing effective conservation practices becomes essential to safeguard intertidal mudflats from the escalating impacts of global warming and subsequent sea level rise.

Methods

The modeling system consisted in a physical-biological coupled model forced by meteorological data simulated by 11 downscaled General Circulation Models-Regional Circulation Models (GCM-RCM) from the Coupled Model Intercomparison Project - Phase 5 (CMIP5) to resolve potential future conditions at the mud surface (Table 1). The GCM-RCM were initially forced by (i) historical greenhouse gases concentrations, (ii) Representative Concentration Pathways (RCP) scenarios, and (iii) theoretical tidal forcings with and without sea level rise[6,17–20]. The physical-biological coupled model simulated mud surface temperature (MST), the biomass and the net primary production (NPP) of microphytobenthos (MPB), and the biomass and secondary production of gastropod *Peringia ulvae*, one main grazer of MPB at our study site. The biological parameters used in this study were derived from a subset of 10,000 Monte Carlo simulations[6]. They closely align with observations from the study site and reflect a consistent behavior of the model. The model was applied on a temperate intertidal mudflat located in NW France (Fig. 1). The code and forcings used in this study are made available in a public Zenodo repository[59] and therefore can be used or further developed by other researchers.

Mud surface temperature model

The heat energy balance was resolved through the first centimeter of the sediment surface[6,60]. During low tides, the equations account for solar and atmospheric downward heat fluxes, upward heat fluxes from the sediment surface, heat conduction between mud and air, and heat fluxes from mud evaporation. During high tides, MST equilibrates with the overlying seawater temperature. Seawater temperature was computed from thermal conduction between air and seawater, upward seawater radiation, and downward solar and atmospheric radiation. Previous in situ-simulated MST comparisons show the good ability of the model to resolve MST[6,21,22]. The MST differential equation was solved with the Euler-Cauchy method with a 30-s time step. The original version of the mud temperature model of ref. 60 is simplified for resolving only the surface temperature during low tides:

$$\rho_M C_{P_M} \frac{\partial T_M(z_0,t)}{\partial t} = f\left(T_M(z_0,t)\right), \tag{1}$$

where $f\left(T_M(z_0,t)\right)$ is the heat energy balance at the sediment surface z_0 (m) at time t (s). The sediment surface layer is 1-cm deep where temperature (K) is assumed homogeneous[61,62]. ρ_M is the volumetric mass of mud (kg m^{-3}) i.e., the sum of the water and dry sediment fractions ($\rho_M = \rho_W\xi + \rho_S(1-\xi)$ where ρ_W and ξ are the water volumetric mass (kg m^{-3}) and the porosity (%), respectively. C_{P_M} is the specific heat capacity of mud at constant pressure (J kg^{-1} K^{-1}):

$$C_{P_M} = \frac{\eta}{\mu\rho_M}, \tag{2}$$

where η is the heat conductivity (W m^{-1} K^{-1}) and μ the thermal diffusivity (m^2 s^{-1}). During low tides, the heat balance is driven by solar and atmospheric radiation (R_S and R_{Atm} in W m^{-2}, respectively), the mud surface (R_M, W m^{-2}), by conductive sensible heat fluxes due to mud-air temperature differences ($S_{Mud\rightarrow Air}$, W m^{-2}) and by evaporative heat flux (V_M, W m^{-2}):

$$f\left(T_M(z_0,t)\right) = R_S + R_{Atm} - R_M - S_{Mud\rightarrow Air} - V_M \text{ with } V_M = \xi V_W, \tag{3}$$

where ξ is the mud porosity ($\xi \in [0, 1]$, %) and V_W is the seawater evaporative heat flux (W m^{-2}).

During high tides, MST quickly reaches the temperature of the overlying water layer[60,61]:

$$T_M(z_0,t) = T_W(t), \tag{4}$$

We computed the temperature of the water column (T_W) from the mixing between the surface layer (z_{top}) and the bottom layer (z_{bot}), where the temperature at the previous time step persists. z_{top} is driven by heat balance at the air-water interface:

$$\rho_W C_{P_W} \frac{\partial T_W(z_{top},t)}{\partial t} = f(T_W(z_{top},t)), \tag{5}$$

$$\text{with } f\left(T_W(z_{top},t)\right) = R_S + R_{Atm} - R_W - S_{Air\rightarrow Water}, \tag{6}$$

where ρ_W is the volumetric mass of water (kg m^{-3}). C_{P_W} is the specific heat capacity of seawater at constant pressure (J kg^{-1} K^{-1}). $T_W(z_{top}, t)$ is the temperature of the surface mixed layer (K). The term $S_{Air\rightarrow Water}$ is the sensible heat flux (W m^{-2}) controlled by the air-water thermal conduction. R_W (W m^{-2}) is the seawater upward radiation.

The surface fraction of the water column influenced by atmospheric forcings is set by α_{top}:

$$\alpha_{top} = 0.15\left(1 + \frac{U}{3}\right), \tag{7}$$

where U is the wind speed (m s^{-1}). The temperature mixing between α_{top} and the remaining part of the water column ($1 - \alpha_{top}$) is set by:

$$T_W(t) = \alpha_{top} T_W(z_{top},t) + \left(1-\alpha_{top}\right) T_W(z_{bot},t) \text{ with } T_W(z_{bot},t) = T_W(t-1) \tag{8}$$

T_W (K) is initially set by:

$$T_W(t) = 18.5 + 5cos\left(2\pi \frac{\text{day} - 230}{\text{year length}}\right) + 273.15, \tag{9}$$

where *day* is the day of the year and the year length is in days.

More details on parameters and constants of the MST model are given in ref. 6.

Biological model

The physical-biological model simulates the MPB biomass and NPP in both the surface of the biofilm and the sediment first centimeter[6]. It also stimulates the biomass and secondary production from *Peringia ulvae*, a very abundant gastropod and important grazer of MPB on the studied mudflat[63]. Exchanges of MPB biomass between the surface of the biofilm and the

sediment first centimeter are ruled by a vertical MPB migration scheme according to diurnal and tidal cycles[6]. At low tides, MPB form a dense active biofilm at the sediment surface during which photosynthetically active radiation (PAR) and MST drives NPP. The grazing rate of *Peringia ulvae* is driven by the simulated MST and MPB biomass in the biofilm. The fourth-order Runge-Kutta method was used to solve the biological differential equations with a 6-min time step.

A system of equations describes the exchanges of MPB biomass between the surface biofilm (S, mg Chl a m^{-2}) and the first cm of sediment (F, mg Chl a m^{-2}) in addition to the biomass of *Peringia ulvae* (Z, mg C m^{-2}) over time. During the daytime low tides:

$$\text{if } \gamma* > 0 \begin{cases} \frac{dS}{dt} = \left(r_F F + P^b S\right)\left(1 - \frac{S}{S_{max}}\right) - m_S S - \left[\text{IR}\left(\frac{Z}{W_Z^{mean}}\right)\right] \times \text{H}\left(S, S_{mini}\right) \\ \frac{dF}{dt} = -r_F F\left(1 - \frac{S}{S_{max}}\right) + P^b S\left(\frac{S}{S_{max}}\right) - m_F F \\ \frac{dZ}{dt} = \theta \times \left[\text{IR}\left(\frac{Z}{W_Z^{mean}}\right)\right] \times \text{H}\left(S, S_{mini}\right) - m_Z Z \\ \frac{d\gamma*}{dt} = -1 \end{cases} \tag{10}$$

$$\text{if } \gamma* \le 0 \begin{cases} \frac{dS}{dt} = -r_S S - m_S S - \left[\text{IR}\left(\frac{Z}{W_Z^{mean}}\right)\right] \times \text{H}\left(S, S_{mini}\right) \\ \frac{dF}{dt} = r_S S - m_F F \\ \frac{dZ}{dt} = \theta \times \left[\text{IR}\left(\frac{Z}{W_Z^{mean}}\right)\right] \times \text{H}\left(S, S_{mini}\right) - m_Z Z \\ \frac{d\gamma*}{dt} = -1 \end{cases} \tag{11}$$

where γ^* (h) determines the duration of the biofilm at the sediment surface. γ^* is set for the next daytime low tide at the end of night-time low tides or high tides (Eqs. (12) and (13))[64,65]. When $\gamma^* > 0$, MPB migrate to the surface biofilm from F to S at a transfer rate of r_F (h^{-1}). The migration stops when S saturates at S_{max} (mg Chl a m^{-2}). NPP occurs only in S and is regulated by the biomass-specific photosynthetic rate P^b (µg C (µg Chl a)$^{-1}$ h^{-1}). NPP is zero when $S = S_{max}$ according to the term $(1 - \frac{S}{S_{max}})$ to account for the carrying capacity in S. When $\gamma^* \le 0$, MPB migrate downward in the sediment from S to F at a rate of r_S (h^{-1}). m_S and m_F are MPB loss rates (h^{-1}) representing senescence and grazing by surface deposit feeders (on S) and subsurface deposit feeders (on F). m_Z is a loss rate (h^{-1}) representing *Peringia ulvae* mortality.

During night-time low tides, MPB migrate into the sediment from S to F. *Peringia ulvae* grazes on remaining MPB in the biofilm (S):

$$\begin{cases} \frac{dS}{dt} = -r_S S - m_S S - \left[\text{IR}\left(\frac{Z}{W_Z^{mean}}\right)\right] \times \text{H}\left(S, S_{mini}\right) \\ \frac{dF}{dt} = r_S S - m_F F \\ \frac{dZ}{dt} = \theta \times \left[\text{IR}\left(\frac{Z}{W_Z^{mean}}\right)\right] \times \text{H}\left(S, S_{mini}\right) - m_Z Z \\ \gamma* = \left(\frac{F}{S_{max}} + 1\right) \times \gamma \end{cases} \tag{12}$$

During high tides, MPB persisting at the surface progressively complete their migration from S to F and *Peringia ulvae* stops grazing:

$$\begin{cases} \frac{dS}{dt} = -r_S S - m_S S \\ \frac{dF}{dt} = r_S S - \nu_F F \\ \frac{dZ}{dt} = -m_Z Z \\ \gamma* = \left(\frac{F}{S_{max}} + 1\right) \times \gamma \end{cases} \tag{13}$$

In the model, MPB are resuspended during high tides at a constant rate. The loss term (ν_F, 0.003 h^{-1}) represents chronic resuspension, senescence and grazing by subsurface deposit feeders. During low tides, loss only accounts for senescence and the grazing by subsurface deposit feeders (m_F, 0.001 h^{-1}).

The biomass-specific photosynthetic rate P^b (µg C (µg Chl a)$^{-1}$ h^{-1}) is regulated by temperature (T, °C) and by photosynthetically active radiation (I, W m^{-2}) i.e., 44 % of downward short-wave radiation[66]. The production rate as a function of I is from ref. 67:

$$P^b = P^b_{\max} \times tanh\left(\frac{I}{I_k}\right), \tag{14}$$

where $P^b_{\max}$ is the photosynthetic capacity (µg C (µg Chl a)$^{-1}$ h^{-1}) and I_k is the light saturation parameter set at 40 W m^{-2}. $P^b_{\max}$ is regulated by MST (T) according to ref. 68:

$$P^b_{\max} = P^b_{MAX} \times \left(\frac{T_{\max} - T}{T_{\max} - T_{opt}}\right)^{\beta} \times e^{\left(-\beta \times \left[\frac{T_{\max} - T}{T_{\max} - T_{opt}} - 1\right]\right)}, \tag{15}$$

where $T_{\max}$ (°C) and T_{opt} (°C) are the maximum and optimal temperature for MPB photosynthesis, respectively. β is a coefficient for the temperature-photosynthesis relationship. P^b_{MAX} is the maximum value of $P^b_{\max}$ at T_{opt}.

The grazing rate of *Peringia ulvae* on S depends on the individual ingestion rate (IR, ng Chl a ind^{-1} h^{-1}) and by the density of *Peringia ulvae* (ind m^{-2}). Grazing is limited to a MPB biomass threshold (S_{mini}, mg Chl a m^{-2}) with an Heaviside function (H). The MPB biomass grazed by Z is partly assimilated into new Z biomass (θ, %). The individual ingestion rate (ng Chl a ind^{-1} h^{-1}) by *Peringia ulvae* follows a sigmoid mathematical function accounting for MST (T, °C):

$$\text{IR} = \text{IR}_{\max} \times \frac{T^{\alpha_Z}}{T^{\alpha_Z} + \left(\frac{T_{opt_Z} + 10}{2}\right)^{\alpha_Z}}, \tag{16}$$

where T_{opt_Z} (°C) is the optimal temperature for grazing. $IR_{\max}$ is the maximal observed individual ingestion rate. α_Z (no unit) is a curvature parameter. The maximal individual ingestion rate $IR_{\max}$ (ng Chl a ind^{-1} h^{-1}) is calculated according to ref. 69. IR_{max} depends on total available MPB biomass:

$$\text{IR}_{\max} = 0.015 \times (F + S)^{1.72} \tag{17}$$

When necessary, Chl a is converted into carbon unit according to a variable C:Chl a ratio (g C g Chl a^{-1}). The ratio is computed according the formulation of Cloern et al.[70]:

$$\frac{Chla}{C} = \left(\frac{Chla}{C}\right)_{\min} \times \left(1 + 4 \times e^{-0.5 \times \frac{I}{K_E}}\right), \tag{18}$$

where $\left(\frac{Chla}{C}\right)_{\min}$ is the minimum Chl a:C ratio (g Chl a g C^{-1}) and K_E, the half-saturation constant for light use (Ein m^{-2} d^{-1}).

Finally, the mortality rate of Z is set by:

$$m_Z = m_Z^{\min} Z, \tag{19}$$

where $m_Z^{\min}$ is the minimum mortality rate (h^{-1}).

The biological model along with parameters values is fully described in ref. 6.

Model forcings

The coupled physical-biological model was forced by the surface atmospheric pressure (Pa), the 2-m specific humidity (kg kg^{-1}), the 2-m air temperature (K), the 10-m wind speed (m s^{-1}), the downwelling shortwave direct radiation (W m^{-2}), the downwelling shortwave scattered radiation (W m^{-2}), and the downwelling longwave radiation (W m^{-2}) extracted with the ADAMONT method[18]. It consisted in a disaggregation method of meteorological parameters from a daily integration period to a hourly time step applied to the 11 GCM-RCM outputs from CMIP5. The GCM-RCM were forced by historical

greenhouse gases concentration (historical run) and RCP scenarios (RCP 4.5 and 8.5 runs; Table 1) on a 8-km horizontal grid encompassing France from 5°W to 12°E and 38°N to 54°N[17,20]. The atmospheric surface pressure was set as constant and the specific humidity was converted into relative humidity from the saturation vapor pressure (e_s) using the Tetens equation for positive and negative temperatures[71–73]. The partial water vapor pressure (e) was then calculated from the specific humidity (q, kg kg^{-1}) and the surface atmospheric pressure (p_{atm}, kPa) as follows:

$$e = \frac{q \times p_{atm}}{0.622 + 0.378 \times q}, \tag{20}$$

and the relative humidity (q_{rel}, %) was then calculated as follows:

$$q_{rel} = \frac{100 \times e}{e_s}. \tag{21}$$

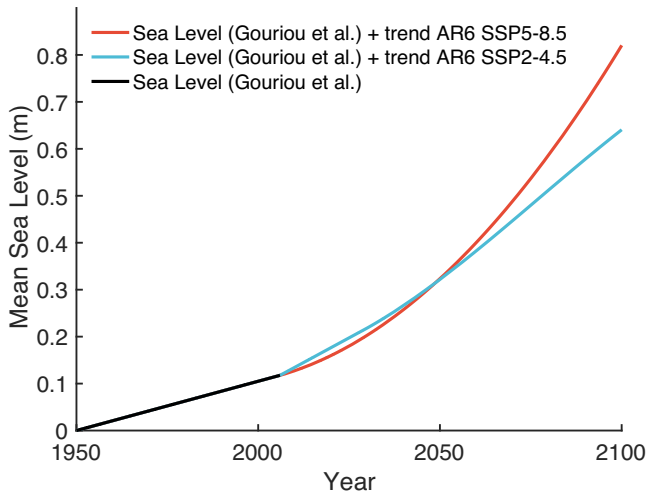

Fig. 4 | Historical and projected mean sea level at La Rochelle-La Pallice tide gauge. Sea level rise at La Rochelle-La Pallice tide gauge station (46°09′30.5″N, 1°13′14.7″W) in the historical (black), SSP 2–4.5 (blue), and SSP 5–8.5 (red) periods according to refs. 75,76.

Regarding the theoretical tidal cycle, a harmonic analysis was first performed over one year of water level measurements measured in 2011 at the Ile d'Aix tide gauge (46°0′26″N, 01°10′27″W) using the U-Tide software[74]. Based on amplitudes and phases of the 59 main tidal constituents, a tidal prediction was then performed over 1950–2100, discarding the linear trend present in the data. The tidal cycle was determined by correcting the tidal height with the bathymetry (3.204 m above chart datum) extracted from a digital elevation model (Litto3D® 2010; Charente Maritime by the Institut National de l'Information Géographique et Forestière (IGN) and the SHOM) at the pixel corresponding to the study site.

Over the historical period (1950–2005), we used the sea level rise trend of +2.1 ± 0.3 mm yr^{-1} as reported by ref. 75, which was derived from the reconstruction of meteorological and tide-gauge archive data in the region. In addition, for the period 2006–2100 we used the sea level rise projections provided in the IPCC Sixth Assessment Report (AR6)[76]. AR6 sea level rise projections account for contributions of sterodynamic processes, melting of the Greenland and Antarctic ice sheets, land water storage changes, vertical land motion signals including both Glacial Isostatic Adjustment and other long-term drivers[76]. We used the 50th percentiles (i.e., median) projections for sea level rise scenarios of SSP 2-4.5 (+0.63 m by 2100), and SSP 5–8.5 (+0.83 m by 2100) at the location of La Rochelle-La Pallice tide gauge station (46°09′30.5″N, 1°13′14.7″W) located within our study area. The long-term sea level rise trend derived from AR6 indicates a projected increase in mean tide levels of 5 % under SSP 2–4.5 and 9% under SSP 5–8.5 from 2006 to 2100, which is used to constrain the tidal prediction results (Fig. 4). Sea level rise can also have a direct impact on tidal range, although to a lesser extent. Along the northwestern Atlantic coast of France, ref. 77 demonstrated that high tide levels could increase by ca. 3% of the sea level rise for scenarios from +1 to +5 m.

The physical-biological model was run over historical (1951–2005) and RCP (2006–2099) periods. We run the model at a site located in the middle shore of the Brouage mudflat (45°54′50″N, 01°05′25″W)[6]. In the historical run, the MPB initial conditions were set to 0 mg Chl *a* m^{-2} and 100 mg Chl *a* m^{-2} in the biofilm and the sediment first centimeter, respectively. For the MPB grazer biomass, we set the initial conditions to 1000 mg C m^{-2} at the sediment surface.

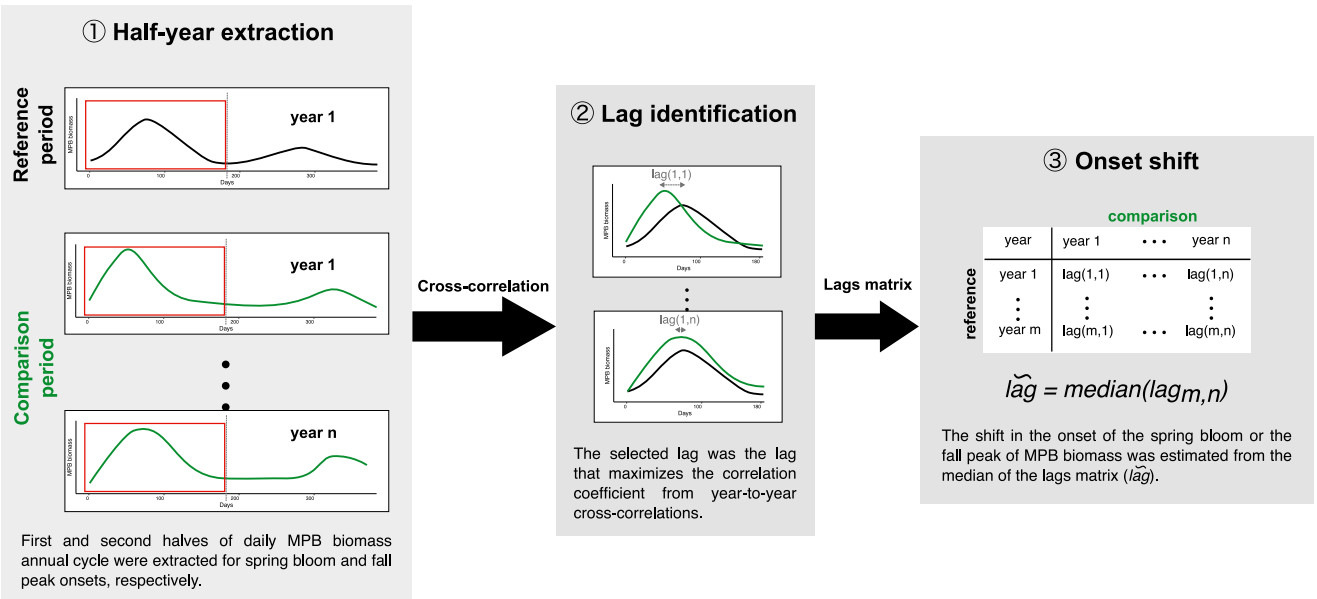

Fig. 5 | Detection method of the MPB phenological shifts using cross-correlation lags. The method uses cross correlation to quantify the MPB phenological shifts by (1) extracting half-years of interest, (2) identifying lags by comparing reference and comparison periods, and (3) estimating shifts from the median of lags.

Table 2 | Time periods compared in year-to-year cross-correlations (without sea level rise)

Comparison	Reference period	Comparison period
Historical vs Historical	1952–1981	1976–2005
Historical vs RCP 4.5	1976–2005	2069–2098
Historical vs RCP 8.5	1976–2005	2069–2098

Post analysis

NPP, secondary production, and irradiance were integrated over seasons (winter: January, February, March; spring: April, May, June; summer: July, August, September; fall: October, November, December) and years. MST was averaged over seasons and years. Daily values of MPB biomass corresponded to the total MPB biomass concentration at noon, every day.

Monotonic trends for the simulated irradiance, MST, NPP, and secondary production were estimated using the non-parametric Mann-Kendall test under the scaling hypothesis[78,79]. As autocorrelation or long-term persistence (LTP) of patterns observed in the past can affect the trend estimation[80], we used the Mann-Kendall LTP function of the Hurst-Kolmogorov (HK) process R package[81]. First, the function tested the significance of the trend based on the Sen slope estimator[82]. If the trend is significant ($p < 0.05$), the Hurst exponent coefficient (H), which is a measure of the long-term persistence, was estimated according to ref. 80. If H is significant ($p < 0.05$), the trend test statistics were corrected from bias introduced by long-term persistence[79]. Depending on the results, the trend significance level was assessed by the p-value from the classical Mann-Kendall test or from the corrected statistics.

We assessed the variability of the onset of the MPB spring and fall blooms by assessing the cross-correlations among years of a of two time periods (Fig. 5 and Table 2). For each pair of GCM-RCM, and for each year, the annual cycle of the simulated daily MPB biomass was divided in halves. Each half was analyzed to identify the onset of the spring and fall blooms, respectively. To compare these periods, the reference period was cross-correlated with all years of the comparison period (Fig. 5). The cross-correlation measured the similarities between the two time series by calculating correlation coefficients distributed across positive and negative time lags in days. The year-to-year temporal shift in the simulated onset of the spring and fall blooms was determined by identifying the lag that maximized the correlation coefficient (Fig. 5). The year-to-year variability was first assessed between the beginning (1952–1981) and the end of historical run (1976–2005) and then between the end of the historical run (1976–2005) and the RCP 4.5 and 8.5 runs (2069–2098; Table 2). Statistical significance of the lag compared to the reference period was tested with Mann–Whitney–Wilcoxon test[78]. We analyzed the ensemble mean of the 11 GCM-RCM pairs. The error bars and ± symbols refer to the confidence interval at 95% of the ensemble mean.

Data availability

Data are available on a public repository: https://doi.org/10.5281/zenodo.11461487.

Code availability

Code is available on a public repository: https://doi.org/10.5281/zenodo.11461487.

Received: 29 August 2023; Accepted: 4 October 2024;
Published online: 19 October 2024

References

1. Finlayson, M. et al. *Millennium Ecosystem Assessment: Ecosystems and Human Well-being: Wetlands and Water Synthesis* (2005).
2. Nicholls, R. et al. In *Climate Change 2007: Impacts, Adaptation and Vulnerability. Contribution of Working Group II to the Fourth Assessment Report of the Intergovernmental Panel on Climate Change* (eds Parry, M. L., Canziani, O. F., Palutikof, J. P., van der Linden, P. J. & Hanson, C. E.) (2007).
3. Foster, N. M., Hudson, M. D., Bray, S. & Nicholls, R. J. Intertidal mudflat and saltmarsh conservation and sustainable use in the UK: a review. *J. Environ. Manag.* **126**, 96–104 (2013).
4. Underwood, G. & Kromkamp, J. Primary production by phytoplankton and microphytobenthos in estuaries. *Adv. Ecol. Res.* **29**, 93–153 (1999).
5. Chavez, F. P., Messié, M. & Pennington, J. T. Marine primary production in relation to climate variability and change. *Annu. Rev. Mar. Sci.* **3**, 227–260 (2011).
6. Savelli, R. et al. On biotic and abiotic drivers of the microphytobenthos seasonal cycle in a temperate intertidal mudflat: a modelling study. *Biogeosciences* **15**, 7243–7271 (2018).
7. Savelli, R. et al. Impact of chronic and massive resuspension mechanisms on the microphytobenthos dynamics in a temperate intertidal mudflat. *J. Geophys. Res.: Biogeosci.* **124**, 3752–3777 (2019).
8. Pinckney, J. L. A mini-review of the contribution of benthic microalgae to the ecology of the continental shelf in the South Atlantic bight. *Estuaries Coasts* **41**, 2070–2078 (2018).
9. Hope, J. A., Paterson, D. M. & Thrush, S. F. The role of microphytobenthos in soft-sediment ecological networks and their contribution to the delivery of multiple ecosystem services. *J. Ecol.* **108**, 815–830 (2020).
10. Park, J. et al. Harnessing the power of tidal flat diatoms to combat climate change. *Crit. Rev. Environ. Sci. Technol.* **54**, 1395–1416 (2024).
11. Christianen, M. J. A. et al. Benthic primary producers are key to sustain the Wadden sea food web: stable carbon isotope analysis at landscape scale. *Ecology* **98**, 1498–1512 (2017).
12. Dubois, S., Orvain, F., Marin-Léal, J. C., Ropert, M. & Lefebvre, S. Small-scale spatial variability of food partitioning between cultivated oysters and associated suspension-feeding species, as revealed by stable isotopes. *Mar. Ecol. Prog. Ser.* **336**, 151–160 (2007).
13. Morioka, H., Kasai, A., Miyake, Y., Kitagawa, T. & Kimura, S. Food composition for blue mussels (Mytilus edulis) in the Menai Strait, UK, based on physical and biochemical analyses. *J. Shellfish Res.* **36**, 659–668 (2017).
14. Underwood, G. In *Encyclopedia of Ocean Sciences* (ed. Steele, J. H.) 1770–1777 (Academic Press, Oxford, 2001).
15. Cabré, A., Marinov, I. & Leung, S. Consistent global responses of marine ecosystems to future climate change across the IPCC AR5 earth system models. *Clim. Dyn.* **45**, 1253–1280 (2015).
16. Henson, S. A., Cael, B., Allen, S. R. & Dutkiewicz, S. Future phytoplankton diversity in a changing climate. *Nat. Commun.* **12**, 1–8 (2021).
17. Vidal, J.-P., Martin, E., Franchistéguy, L., Baillon, M. & Soubeyroux, J.-M. A 50-year high-resolution atmospheric reanalysis over France with the Safran system. *Int. J. Climatol.* **30**, 1627–1644 (2010).
18. Verfaillie, D., Déqué, M., Morin, S. & Lafaysse, M. The method Adamont v1. 0 for statistical adjustment of climate projections applicable to energy balance land surface models. *Geosci. Model Dev.* **10**, 4257–4283 (2017).
19. Taylor, K. E., Stouffer, R. J. & Meehl, G. A. An overview of cmip5 and the experiment design. *Bull. Am. Meteorol. Soc.* **93**, 485–498 (2012).
20. Pachauri, R. K. et al. *Climate Change 2014 Synthesis Report. Contribution of working groups I, II, and III to the Fifth Assessment Report of the Intergovernmental Panel on Climate Change* (2014).
21. Méléder, V. et al. Mapping the intertidal microphytobenthos gross primary production part I: coupling multispectral remote sensing and physical modeling. *Front. Mar. Sci.* **7**, 520 (2020).
22. Savelli, R. et al. Mapping the intertidal microphytobenthos gross primary production, part II: merging remote sensing and physical-biological coupled modeling. *Front. Mar. Sci.* **7**, 521 (2020).
23. Laufkötter, C. et al. Drivers and uncertainties of future global marine primary production in marine ecosystem models. *Biogeosciences* **12**, 6955–6984 (2015).

24. Tagliabue, A. et al. Persistent uncertainties in ocean net primary production climate change projections at regional scales raise challenges for assessing impacts on ecosystem services. *Front. Clim.* **3**, 738224 (2021).
25. Brito, A. C. et al. Seasonality of microphytobenthos revealed by remote-sensing in a south European estuary. *Cont. Shelf Res.* **66**, 83–91 (2013).
26. Haro, S. et al. Microbenthic net metabolism along intertidal gradients (Cadiz Bay, SW Spain): spatio-temporal patterns and environmental factors. *Front. Mar. Sci.* **7**, 39 (2020).
27. Morim, J. et al. Robustness and uncertainties in global multivariate wind-wave climate projections. *Nat. Clim. Change* **9**, 711–718 (2019).
28. Ruosteenoja, K., Vihma, T. & Venäläinen, A. Projected changes in European and North Atlantic seasonal wind climate derived from cmip5 simulations. *J. Clim.* **32**, 6467–6490 (2019).
29. Cartaxana, P. et al. Physiological versus behavioral photoprotection in intertidal epipelic and epipsammic benthic diatom communities. *J. Exp. Mar. Biol. Ecol.* **405**, 120–127 (2011).
30. Vieira, S., Cartaxana, P., Máguas, C. & Marques da Silva, J. Photosynthesis in estuarine intertidal microphytobenthos is limited by inorganic carbon availability. *Photosynth. Res.* **128**, 85–92 (2016).
31. Vopel, K., Del-Río, C. & Pilditch, C. A. Effects of CO_2 enrichment on benthic primary production and inorganic nitrogen fluxes in two coastal sediments. *Sci. Rep.* **8**, 1–15 (2018).
32. Petrou, K. et al. Acidification diminishes diatom silica production in the southern ocean. *Nat. Clim. Change* **9**, 781–786 (2019).
33. Regnier, P. et al. Anthropogenic perturbation of the carbon fluxes from land to ocean. *Nat. Geosci.* **6**, 597–607 (2013).
34. Yang, Q. et al. Increased nitrogen export from eastern North America to the Atlantic Ocean due to climatic and anthropogenic changes during 1901–2008. *J. Geophys. Res.: Biogeosci.* **120**, 1046–1068 (2015).
35. Maavara, T., Lauerwald, R., Regnier, P. & Van Cappellen, P. Global perturbation of organic carbon cycling by river damming. *Nat. Commun.* **8**, 15347 (2017).
36. Hicks, N. et al. Temperature driven changes in benthic bacterial diversity influences biogeochemical cycling in coastal sediments. *Front. Microbiol.* **9**, 1730 (2018).
37. Cadée, G. & Hegeman, J. Primary production of the benthic microflora living on tidal flats in the Dutch Wadden Sea. *Neth. J. Sea Res.* **8**, 260–291 (1974).
38. Cariou-Le Gall, V. & Blanchard, G. Monthly HPLC measurements of pigment concentration from an intertidal muddy sediment of Marennes-Oléron Bay, France. *Mar. Ecol. Prog. Ser.* **121**, 171–179 (1995).
39. Sahan, E. et al. Community structure and seasonal dynamics of diatom biofilms and associated grazers in intertidal mudflats. *Aquat. Microb. Ecol.* **47**, 253–266 (2007).
40. Orvain, F., Guizien, K., Lefebvre, S., Bréret, M. & Dupuy, C. Relevance of macrozoobenthic grazers to understand the dynamic behaviour of sediment erodibility and microphytobenthos resuspension in sunny summer conditions. *J. Sea Res.* **92**, 46–55 (2014).
41. Brown, J. H., Gillooly, J. F., Allen, A. P., Savage, V. M. & West, G. B. Toward a metabolic theory of ecology. *Ecology* **85**, 1771–1789 (2004).
42. López-Urrutia, Á., San Martin, E., Harris, R. P. & Irigoien, X. Scaling the metabolic balance of the oceans. *Proc. Natl Acad. Sci. USA* **103**, 8739–8744 (2006).
43. Philippe, A. S. et al. Building a database for long-term monitoring of benthic macrofauna in the Pertuis-Charentais (2004–2014). *Biodivers. Data J.* **5**, e10288 (2017).
44. Nguyen, H. T. et al. Persistent benthic communities in the extreme dynamic intertidal mudflats of the Amazonian coast: an overview of the Tanaidacea (Crustacea, Peracarida). *Mar. Biodivers.* **48**, 1841–1853 (2018).
45. Poloczanska, E. S. et al. Responses of marine organisms to climate change across oceans. *Front. Mar. Sci.* **3**, 62 (2016).
46. Yamaguchi, R. et al. Trophic level decoupling drives future changes in phytoplankton bloom phenology. *Nat. Clim. Change* **12**, 469–476 (2022).
47. Cushing, D. Plankton production and year-class strength in fish populations: an update of the match/mismatch hypothesis. *Adv. Mar. Biol.* **26**, 249–293 (1990).
48. Philippart, C. J. et al. Climate-related changes in recruitment of the bivalve Macoma balthica. *Limnol. Oceanogr.* **48**, 2171–2185 (2003).
49. Edwards, M. & Richardson, A. J. Impact of climate change on marine pelagic phenology and trophic mismatch. *Nature* **430**, 881–884 (2004).
50. Moore, P. J., Thompson, R. C. & Hawkins, S. J. Phenological changes in intertidal con-specific gastropods in response to climate warming. *Glob. Change Biol.* **17**, 709–719 (2011).
51. Atkinson, A. et al. Questioning the role of phenology shifts and trophic mismatching in a planktonic food web. *Prog. Oceanogr.* **137**, 498–512 (2015).
52. Delaporte, M. et al. Impact of food availability on energy storage and defense related hemocyte parameters of the Pacific oyster Crassostrea gigas during an experimental reproductive cycle. *Aquaculture* **254**, 571–582 (2006).
53. Studds, C. E. et al. Rapid population decline in migratory shorebirds relying on yellow sea tidal mudflats as stopover sites. *Nat. Commun.* **8**, 14895 (2017).
54. Jourdan, C. et al. Daytime, tidal amplitude and protected areas influence movements and habitat use on mudflats of wintering black-tailed godwits. *Estuar., Coast. Shelf Sci.* **268**, 107782 (2022).
55. McGrath, L. J., Van Riper III, C. & Fontaine, J. J. Flower power: tree flowering phenology as a settlement cue for migrating birds. *J. Animal Ecol.* **78**, 22–30 (2009).
56. Bowgen, K. M., Stillman, R. A. & Herbert, R. J. Predicting the effect of invertebrate regime shifts on wading birds: insights from Poole harbour, UK. *Biol. Conserv.* **186**, 60–68 (2015).
57. Booty, J. M., Underwood, G. J. C., Parris, A., Davies, R. G. & Tolhurst, T. J. Shorebirds affect ecosystem functioning on an intertidal mudflat. *Front. Mar. Sci.* **7**, 685 (2020).
58. Canham, R., Rourke, J. & Ydenberg, R. C. The exploitation of biofilm by migrant western sandpipers (Calidris mauri). *Heliyon* **9**, e17268 (2023).
59. Savelli, R. et al. Warming could shift the phenological responses of benthic microalgae in temperate intertidal zones. https://doi.org/10.5281/zenodo.11461487 (2024).
60. Guarini, J.-M., Blanchard, G. F., Gros, P. & Harrison, S. Modelling the mud surface temperature on intertidal flats to investigate the spatio-temporal dynamics of the benthic microalgal photosynthetic capacity. *Mar. Ecol. Prog. Ser.* **153**, 25–36 (1997).
61. Harrison, S. & Phizacklea, A. Vertical temperature gradients in muddy intertidal sediments in the Forth estuary, Scotland 1. *Limnol. Oceanogr.* **32**, 954–963 (1987).
62. Piccolo, M., Perillo, G. & Daborn, G. Soil temperature variations on a tidal flat in Minas Basin, Bay of Fundy, Canada. *Estuar., Coast. Shelf Sci.* **36**, 345–357 (1993).
63. Sauriau, P.-G., Mouret, V. & Rince, J.-P. Trophic system of wild soft-bottom molluscs in the Marennes-Oleron oyster-farming bay. *Oceanol. Acta Paris* **12**, 193–204 (1989).
64. Guarini, J.-M., Sari, N. & Moritz, C. Modelling the dynamics of the microalgal biomass in semi-enclosed shallow-water ecosystems. *Ecol. Model.* **211**, 267–278 (2008).
65. Guarini, J.-M., Blanchard, G. & Richard, P. In *Functioning of Microphytobenthos in Estuaries* 187–226 (2006).
66. Britton, C. & Dodd, J. Relationships of photosynthetically active radiation and shortwave irradiance. *Agric. Meteorol.* **17**, 1–7 (1976).

67. Platt, T. & Jassby, A. D. The relationship between photosynthesis and light for natural assemblages of coastal marine phytoplankton 1. *J. Phycol.* **12**, 421–430 (1976).
68. Blanchard, G., Guarini, J.-M., Richard, P., Ph, G. & Mornet, F. Quantifying the short-term temperature effect on light-saturated photosynthesis of intertidal microphytobenthos. *Mar. Ecol. Prog. Ser.* **134**, 309–313 (1996).
69. Haubois, A.-G., Sylvestre, F., Guarini, J.-M., Richard, P. & Blanchard, G. Spatio-temporal structure of the epipelic diatom assemblage from an intertidal mudflat in Marennes-Oléron Bay, France. *Estuar., Coast. Shelf Sci.* **64**, 385–394 (2005).
70. Cloern, J. E., Grenz, C. & Vidergar-Lucas, L. An empirical model of the phytoplankton chlorophyll: carbon ratio-the conversion factor between productivity and growth rate. *Limnol. Oceanogr.* **40**, 1313–1321 (1995).
71. Tetens, O. Uber einige meteorologische begriffe. *Z. Geophys* **6**, 297–309 (1930).
72. Monteith, J. L. & Unsworth, M. *Principles of Environmental Physics* (2008).
73. Murray, F. W. *On the Computation of Saturation Vapor Pressure*. Tech. Rep., Rand Corp Santa Monica Calif (1966).
74. Codiga, D. L. *Unified Tidal Analysis and Prediction Using the UTide Matlab Functions* (2011).
75. Gouriou, T., Míguez, B. M. & Wöppelmann, G. Reconstruction of a two-century long sea level record for the Pertuis d'Antioche (France). *Cont. Shelf Res.* **61**, 31–40 (2013).
76. Fox-Kemper, B. et al. Ocean, cryosphere and sea level change. In *Climate Change 2021: The Physical Science Basis. Contribution of Working Group I to the Sixth Assessment Report of the Intergovernmental Panel on Climate Change*, Chap. 9, 1211–1362 (Cambridge University Press, 2021).
77. Idier, D., Paris, F., Cozannet, G. L., Boulahya, F. & Dumas, F. Sea-level rise impacts on the tides of the European shelf. *Cont. Shelf Res.* **137**, 56–71 (2017).
78. Mann, H. B. Nonparametric tests against trend. *Econometrica: J. Econom. Soc.* **13**, 245–259 (1945).
79. Kendall, M. G. *Rank Correlation Methods* (1948).
80. Hamed, K. H. Trend detection in hydrologic data: the Mann–Kendall trend test under the scaling hypothesis. *J. Hydrol.* **349**, 350–363 (2008).
81. Tyralis, H. Hkprocess: Hurst-Kolmogorov process. R package version 0.0-2 (2016).
82. Sen, P. K. Estimates of the regression coefficient based on Kendall's tau. *J. Am. Stat. Assoc.* **63**, 1379–1389 (1968).
83. Hulskamp, R. et al. Global distribution and dynamics of muddy coasts. *Nat. Commun.* **14**, 8259 (2023).
84. Group, G. B. C. *The GEBCO_2023 Grid—A Continuous Terrain Model of the Global Oceans and Land*. Liverpool, UK, British Oceanographic Data Centre, National Oceanography Centre, NERC (2023).

Acknowledgements

The authors acknowledge Météo-France for providing the meteorological data and the Service Hydrographique et Océanographique de la Marine (SHOM) for providing the digital elevation model. The authors also thank X. Bertin (LIENSs) for providing the tidal prediction from 1950 to 2100 and D. Idier (BRGM) for discussing on the potential changes in tidal range along the French Atlantic coast. We are very grateful for the Editor and reviewers' feedback, which significantly enhanced the manuscript. This research was funded by the Centre National d'Etudes Spatiales (CNES), the Centre National de la Recherche Scientifique (CNRS, LEFE-EC2CO program), the Région Nouvelle-Aquitaine, and the European Commission (CPER/FEDER). VLF received support from funding provided by the REWRITE project, which has received funding from the European Union's Horizon Europe research and innovation programme under the grant agreement N°101081357. As part of the La Rochelle Territoire Zéro Carbone (LRTZC) initiative, VLF and CD received support from funding provided by the Plan d'Investissement d'Avenir (PIA) through the Territoires d'Innovation de Grande Envergure (TIGA), managed by the Caisse des Dépôts, as well as from the Région Nouvelle-Aquitaine (grant agreement 25875420). RS was supported by a postdoctoral fellowship from Caltech-NASA Jet Propulsion Laboratory (USA). The research was carried out at the Jet Propulsion Laboratory, California Institute of Technology, under a contract with the National Aeronautics and Space Administration (80NM0018D0004). © 2024. All rights reserved.

Author contributions

Conceptualization: V. Le Fouest and R. Savelli. Data curation: R. Savelli, G. Perrois, and F. Rousset. Funding acquisition: V. Le Fouest and C. Dupuy. Methodology: R. Savelli, V. Le Fouest, M. Becker, and F. Rousset. Software: R. Savelli, V. Le Fouest, and G. Perrois. Validation: R. Savelli and V. Le Fouest. Writing—original draft: R. Savelli, V. Le Fouest, M. Becker, and C. Dupuy. Formal analysis: R. Savelli, V. Le Fouest, and G. Perrois. Investigation: R. Savelli, V. Le Fouest, and G. Perrois. Project administration: V. Le Fouest and C. Dupuy. Resources: V. Le Fouest and C. Dupuy. Supervision: V. Le Fouest, C. Dupuy, D. Menemenlis, and M. Simard. Visualization: R. Savelli and G. Perrois. Writing—review & editing: R. Savelli, V. Le Fouest, M. Becker, C. Dupuy, and M. Simard.

Competing interests

The authors declare no competing interests.

Additional information

Supplementary information The online version contains supplementary material available at https://doi.org/10.1038/s43247-024-01764-2.

Correspondence and requests for materials should be addressed to Raphaël. Savelli.

Peer review information *Communications Earth & Environment* thanks the anonymous reviewers for their contribution to the peer review of this work. Primary Handling Editors: Huai Chen, Clare Davis, Martina Grecequet, and Aliénor Lavergne. A peer review file is available.